

## Verification of the Hyperplastic Material Model with Damage for Woven Composites by Experimental Measurements Using Digital Image Correlation

MANDYS T.<sup>1,a</sup>, LAŠ V.<sup>1,b</sup>, KROUPA T.<sup>1,c</sup>, LOBOVSKÝ L.<sup>1,d</sup>

<sup>1</sup>University of West Bohemia in Pilsen, NTIS – New Technologies for Information Society,  
Technická 8, 301 00 Pilsen, Czech Republic

<sup>a</sup>tmandys@ntis.zcu.cz, <sup>b</sup>las@ntis.zcu.cz, <sup>c</sup>kroupa@ntis.zcu.cz, <sup>d</sup>lobo@ntis.zcu.cz

**Keywords:** Woven composite, Digital image correlation, Experiment, Damage, Elasto-plastic

**Abstract.** The paper is aimed at testing the newly developed elasto-plastic material model with damage for the description of non-linear mechanical behaviour of the woven composites. Capabilities of the material model are verified by the usage of the experimental testing of the specimens with the geometry providing the complex combination of the plastic deformation and material damage during the tensile loading. The results of the numerical simulations are compared to the experimental data analysed by means of digital image correlation.

### Introduction

Composite materials have found widespread applications in the entire sector of transport industry in the current time. It is due to their advantages such as high strength to weight ratio, high stiffness to weight ratio, corrosion resistance and flexibility in the final product design. The main disadvantage of these materials is their susceptibility to the occurrence of damage that causes the irreversible reduction of their stiffness during the loading and affects negatively the lifetime of the composite product. Based on the experimental analysis of the fiberglass woven composites, their non-linear behaviour is most evident during the in-plane shear testing but it can be also found in warp and weft direction during the tensile loading too [1]. A suitability of the usage of composite materials for new industrial applications is usually verified by numerical simulations. Material models used for the modelling of the behaviour of the composite materials are most often based on the linear elastic models of the orthotropic material in commercial finite-element software. Extending the knowledge and using more advanced material models, that are more consistent with the real behaviour of the composite materials, will lead to other expansion of their application.

The hyperplastic material model with damage based on the thermodynamic principles was developed by the authors in order to describe the non-linear behaviour of the woven composites. The mathematical background of the used material model with the relations and the equations including the computational principles and principles of material parameters determination are published in [2]. This material model considers the additive decomposition of the total logarithmic strain tensor to the elastic and the plastic strain tensor in the finite strain theory in accordance with the work [3]. The degradation functions used in the material model and dependent on the elastic strains were proposed for description of the damage states of the modelled material. The applied damage evolution equations in the material model are in accordance with the principles of continuum damage mechanics [4]. Authors proposed material model was then implemented into the finite-element software Abaqus 6.14 using material subroutines UMAT and VUMAT written in Fortran code too.

## Woven composite

The examined woven composite of the total thickness 0.9 mm was made of three layers of plain weave fiberglass fabric with the material density 816 g/m<sup>2</sup> and epoxy resin with designation Epicote MGS 385LR. Experimental cyclic static tensile and compressive tests were performed on the material specimens in accordance with ASTM standards. Material parameters of the woven composite material were identified using mathematical optimization, the principles and the real execution of that are described in [2]. The material parameters are summarized in Tables 1 and 2 [2].

Table 1: Elastic and strain-hardening curve parameters

$E_{11}$	$E_{22}$	$E_{33}$	$G_{12}$	$G_{13}$	$G_{23}$	$\nu_{12}$	$\nu_{23}$	$\nu_{31}$	$R_0$	$K_R$	$n_R$
[GPa]	[GPa]	[GPa]	[GPa]	[GPa]	[GPa]	[-]	[-]	[-]	[MPa]	[MPa]	[-]
25.30	25.79	8.00	4.50	4.50	2.75	0.337	0.337	0.280	35	265	0.4

Table 2: Material damage parameters, units [-]

$\epsilon_{11_T}^0$	$\epsilon_{11_C}^0$	$\epsilon_{22_T}^0$	$\epsilon_{22_C}^0$	$\epsilon_{33_T}^0$	$\epsilon_{33_C}^0$	$\gamma_{12}^0$	$\gamma_{23}^0$	$\gamma_{13}^0$
0.0030	0.0007	0.0040	0.0076	0.0	0.0076	0.0048	0.0	0.0
$\epsilon_{11_T}^R$	$\epsilon_{11_C}^R$	$\epsilon_{22_T}^R$	$\epsilon_{22_C}^R$	$\epsilon_{33_T}^R$	$\epsilon_{33_C}^R$	$\gamma_{12}^R$	$\gamma_{23}^R$	$\gamma_{13}^R$
0.0084	0.0500	0.0060	0.0500	0.0001	0.0500	0.0102	0.0001	0.0001
$\epsilon_{11_T}^F$	$\epsilon_{11_C}^F$	$\epsilon_{22_T}^F$	$\epsilon_{22_C}^F$	$\epsilon_{33_T}^F$	$\epsilon_{33_C}^F$	$\gamma_{12}^F$	$\gamma_{23}^F$	$\gamma_{13}^F$
0.0125	0.2000	0.0137	0.2000	0.0233	0.2000	0.0391	0.0350	0.0350
$a_{11_T}$	$a_{11_C}$	$a_{22_T}$	$a_{22_C}$	$a_{33_T}$	$a_{33_C}$	$a_{44}$	$a_{55}$	$a_{66}$
0.0125	0.2000	0.0137	0.2000	0.0233	0.2000	0.50	0.50	0.50
$b_{11_T}$	$b_{11_C}$	$b_{22_T}$	$b_{22_C}$	$b_{33_T}$	$b_{33_C}$	$b_{44}$	$b_{55}$	$b_{66}$
0.0	10.0	0.0	10.0	100.0	10.0	100.0	100.0	0.8550
$K_{11_T}^0$	$K_{11_C}^0$	$K_{22_T}^0$	$K_{22_C}^0$	$K_{33_T}^0$	$K_{33_C}^0$	$K_{44}$	$K_{55}$	$K_{66}$
1.0	1.0	1.0	1.0	0.0	1.0	0.0	0.0	0.76
$K_{11_T}^0$	$K_{11_C}^0$	$K_{22_T}^0$	$K_{22_C}^0$	$K_{33_T}^0$	$K_{33_C}^0$	$K_{44}$	$K_{55}$	$K_{66}$
1.0	1.0	1.0	1.0	0.0	1.0	0.0	0.0	0.76
$D_{11_T}^U$	$D_{11_C}^U$	$D_{22_T}^U$	$D_{22_C}^U$	$D_{33_T}^U$	$D_{33_C}^U$	$D_{44}^U$	$D_{55}^U$	$D_{66}^U$
0.1290	0.7500	0.1210	0.75	1.0	0.75	1.0	1.0	1.0
$D_{12}^U$	$D_{13}^U$	$D_{23}^U$	$D_{ij_T}^{\max}$	$D_{ij_C}^{\max}$				
1.0	1.0	1.0	1.0	0.75				

## Testing of the capabilities of the material model

The proposed material model was verified using tests on complex geometries. The planar specimens from woven composite with the total dimension of 160 x 50 mm and five circular perforations were prepared and subjected to tensile loading. All dimensions of the specimen geometry and setup from experimental testing are displayed in Fig. 1. The perforation of the specimens causes a complex combination of the damage states and the plastic deformation of the material during the loading. The investigated area of the specimens is bounded by the extensometer arms. Four types of specimens differing by the angle  $\varphi$  representing the angle between the loading direction and the material direction 1 (warp fibers direction) were tested. The denoting of the specimens was realized according to the value of  $\varphi = 0^\circ, 15^\circ, 30^\circ$  and  $45^\circ$  as TH-0, TH-15, TH-30 and TH-45. The testing machine Zwick Roell Z050 was used to exert

the tensile loading with the velocity  $v = 1.0$  mm/min. The loading state was performed until the visual rupture of the specimens and decrease of the loading force to 20% of its maximal value.

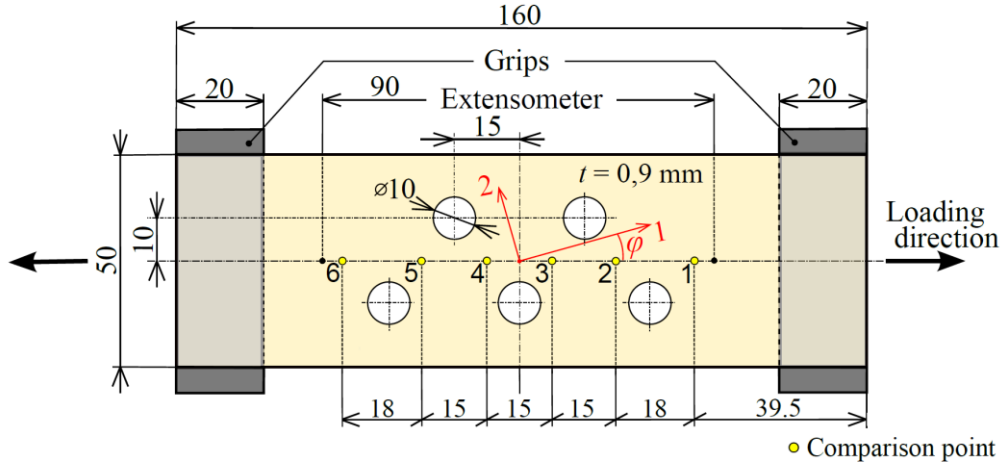


Fig. 1: The perforated specimen geometry and the experimental setup

Distribution of the principal true strain along the perforated specimen's surface during the tensile loading was analyzed by the non-contact and non-destructive technique of digital image correlation (DIC). The DIC optical system consist of the four digital high resolution cameras (4 MPix) was used for the strain distribution analysis based on image captured with frequency of 0.2 Hz. Alternatively, a strong source of light was applied in order to backlight illuminate the fiberglass specimens which are translucent and the permanent structural changes and damage occurred in the material during the tensile loading was captured by the cameras. Three of each type of the perforated specimens were tested and analyzed. The obtained results were compared with results of the corresponding numerical simulations. The element deletion and the finite strain theory were assumed in the case of numerical simulation.

The force-displacement curves obtained from experimental measurement and numerical simulations are compared for the perforated specimens TH-0 and TH-15 in Fig. 2. The same is shown for the specimens TH-30 and TH-45 in Fig. 3. The experimentally recorded force-displacement dependencies showing the relation between the loading force and displacement from the extensometer ( $u$ ) were not post-processed. The black curves correspond to the experimental runs when DIC analysis was applied. The grey curves display the experimental results when the backlight illumination of the specimen was employed.

The strain distribution during the loading was analyzed in the form of the true principal strains (logarithmic strains) along the entire surface of the specimen. In addition, strain-displacement relations were post-processed at six selected points on the surface of the perforated specimen. The location of these comparison points is depicted in Fig. 1. The strain-displacement curves are shown for the selected point no. 2 (see Fig. 1) for all tested specimens TH0 - TH45 in Fig. 4 and Fig. 5. Results for both the maximum ( $\varepsilon_1$ ) and minimum ( $\varepsilon_2$ ) true principal strain are presented. The value of displacement reflects the total displacement of the grips of the testing machine ( $u_i$ ) (which is different from displacement  $u$  measured by the extensometer and used in the force-displacement plots. The numerical results were computed at the selected point using the interpolation from the neighbourhood nodes of the computational mesh. The Fig. 6 – Fig. 13 show a visual comparison of the strain distribution along the specimen surface as a result of the tests with backlight illumination, the tests with the DIC analysis and numerical simulation for all specimen types TH0 - TH45. The comparison is provided always for two cases of loading states of each specimen type. Namely

the state when the specimen is loaded by the maximal loading force and the state when the rupture of the specimens occurs. The first true principal strain  $\epsilon_1$  (maximum true principal strain, logarithmic strain 1) is shown in all cases of visual comparisons.

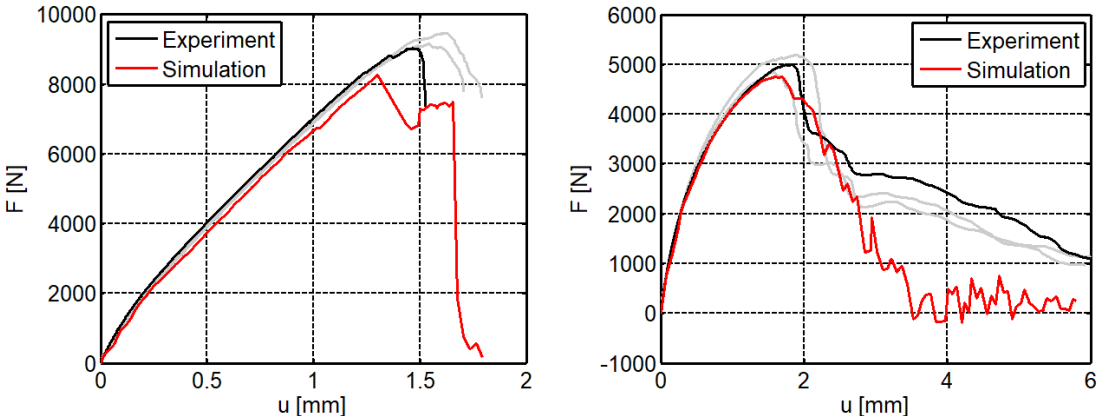


Fig. 2: Force-displacement diagram comparison between experimental and numerical results for specimens TH-0 (left) and TH-15 (right)

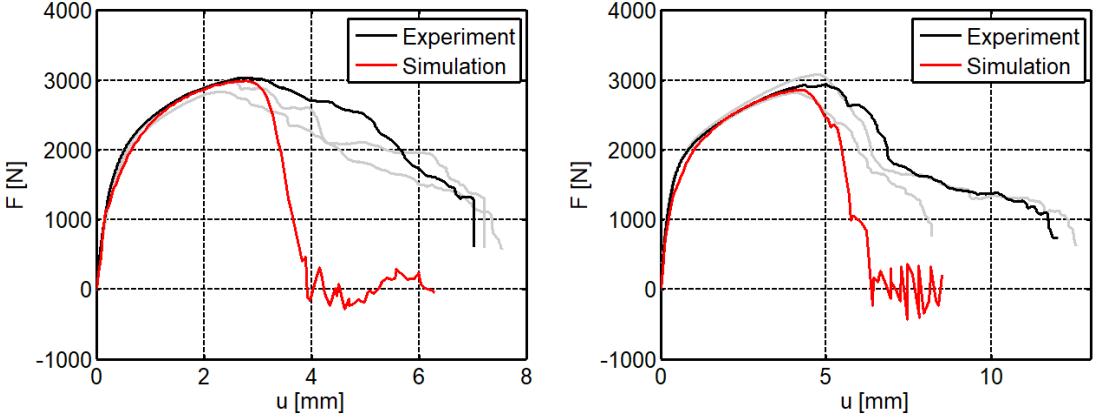


Fig. 3: Force-displacement diagram comparison between experimental and numerical results for specimens TH-30 (left) and TH-45 (right)

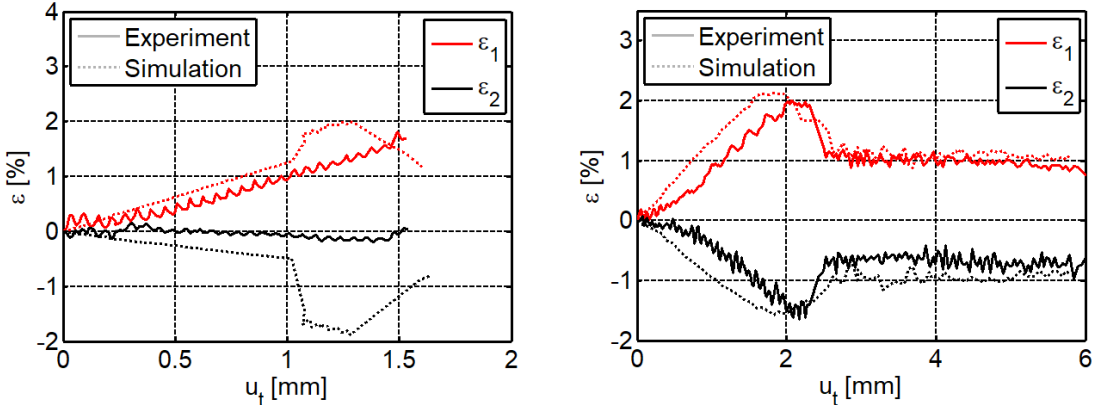


Fig. 4: Relation between the true principal strains (maximum  $\epsilon_1$  and minimum  $\epsilon_2$  true principal strain) and the total displacement for specimens TH-0 (left) and TH-15 (right), comparison between experimental and computational results at point no. 2

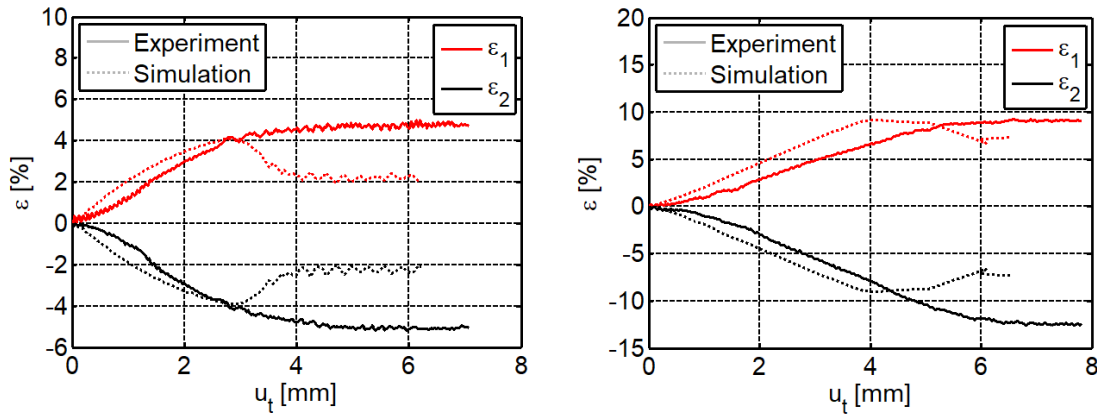


Fig. 5: Relation between the true principal strains (maximum  $\varepsilon_1$  and minimum  $\varepsilon_2$  true principal strain) and the total displacement for specimens TH-30 (left) and TH-45 (right), comparison between experimental and computational results at point no. 2

## Conclusion

The proposed hyperplastic material model with damage for woven composites was verified based on the experimental measurements of the specimens with complex geometry. The material model is implemented into commercial FEM software Abaqus and provides results which correspond well to the recorded experimental data. The force-displacement curves, the strain-displacement relations at selected points, the contour plots of the strain distribution along the specimens surface and the material damage were evaluated and the computational results reflects well experimental data. The force-displacement curves show minimal difference between the experiments and numerical simulations for loading up to the maximal force. The total ruptures of the specimens occur in the case of the numerical simulations but not in the case of experiment, where the damaged specimens show the fiber bridging between individual damaged parts of the specimens. This fact is also evident on the plots of the strain-displacement relation, where the trend diversities occur after the maximal force is reached. The visual comparison of the contour plots of the true strain and of the locations with the material damage provide a qualitative as well as quantitative agreement between experimental and numerical data for all types of the tested specimens.

## Acknowledgment

This publication was supported by the project LO1506 of the Czech Ministry of Education, Youth and Sports and by the project SGS–2019–009.

## References

- [1] T. Kroupa, K. Kunc, R. Zemčík, T. Mandys, The non-linear finite element simulations of tensile tests of textile composites, *Materiali in Technologie* 49 (2015), 509-514.
- [2] T. Mandys, T. Kroupa, V. Laš, L. Lobovský, Hyperplastic material model with damage for woven composites, *Composite Science and Technology* 183 (2019), online.
- [3] M.Á. Caminero, F.J. Montáns, K.J. Bathe, Modeling large strain anisotropic elastoplasticity with logarithmic strain and stress measure, *Computers & Structures* 89 (2011), 826-843.
- [4] S. Murakami, *Continuum Damage Mechanics – A continuum Mechanics Approach to the Analysis of Damage and Fracture*, Springer Science + Business Media press, 2012.

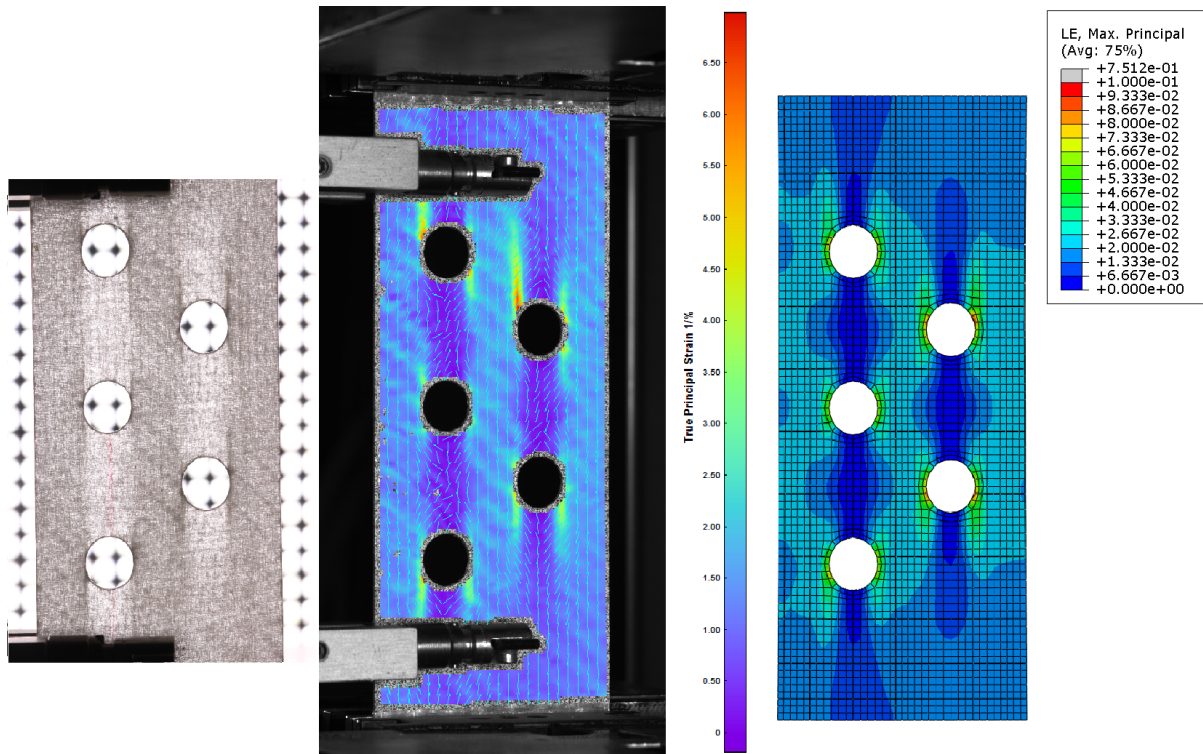


Fig. 6: Visual comparison of results for specimen TH-0 and loading force  $F = 8000 \text{ N}$  ( $u = 1.2 \text{ mm}$ ): the backlight illuminated specimen (left), the maximum true principal strain as resolved by the DIC system (center) and as computed by the numerical simulation (right)

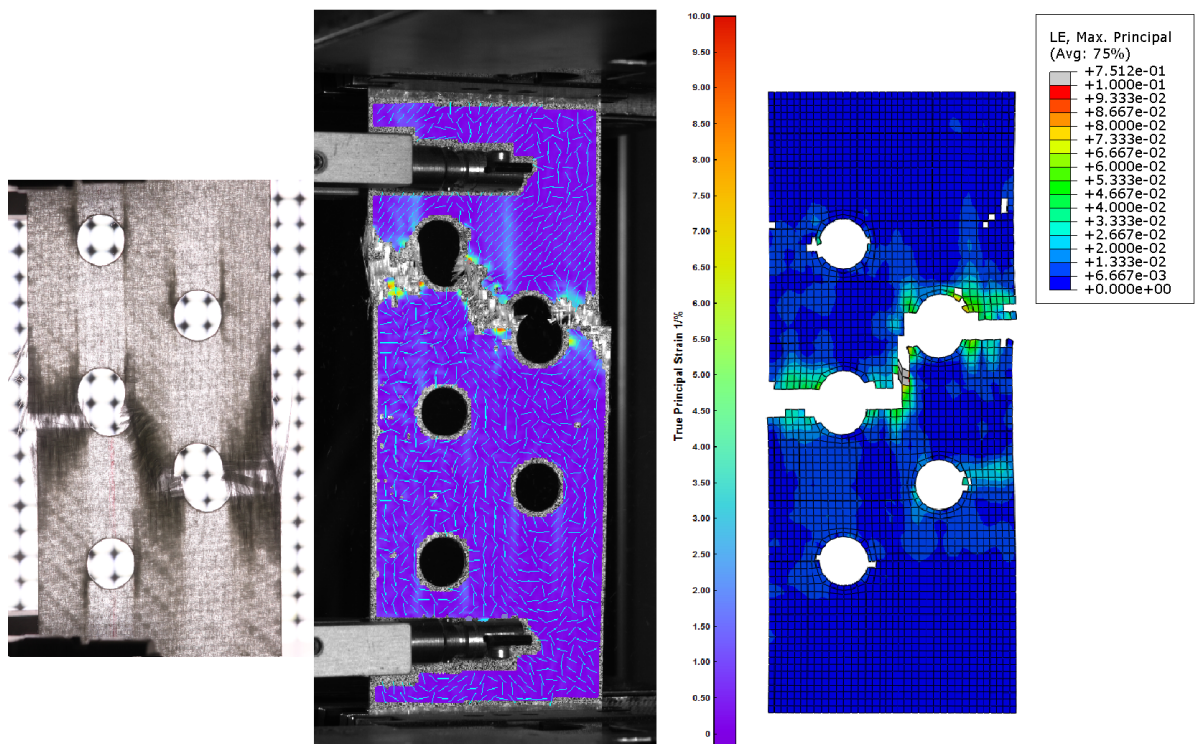


Fig. 7: Visual comparison of results for specimen TH-0 at the end of loading: the backlight illuminated specimen (left), the maximum true principal strain as resolved by the DIC system (center) and as computed by the numerical simulation (right)

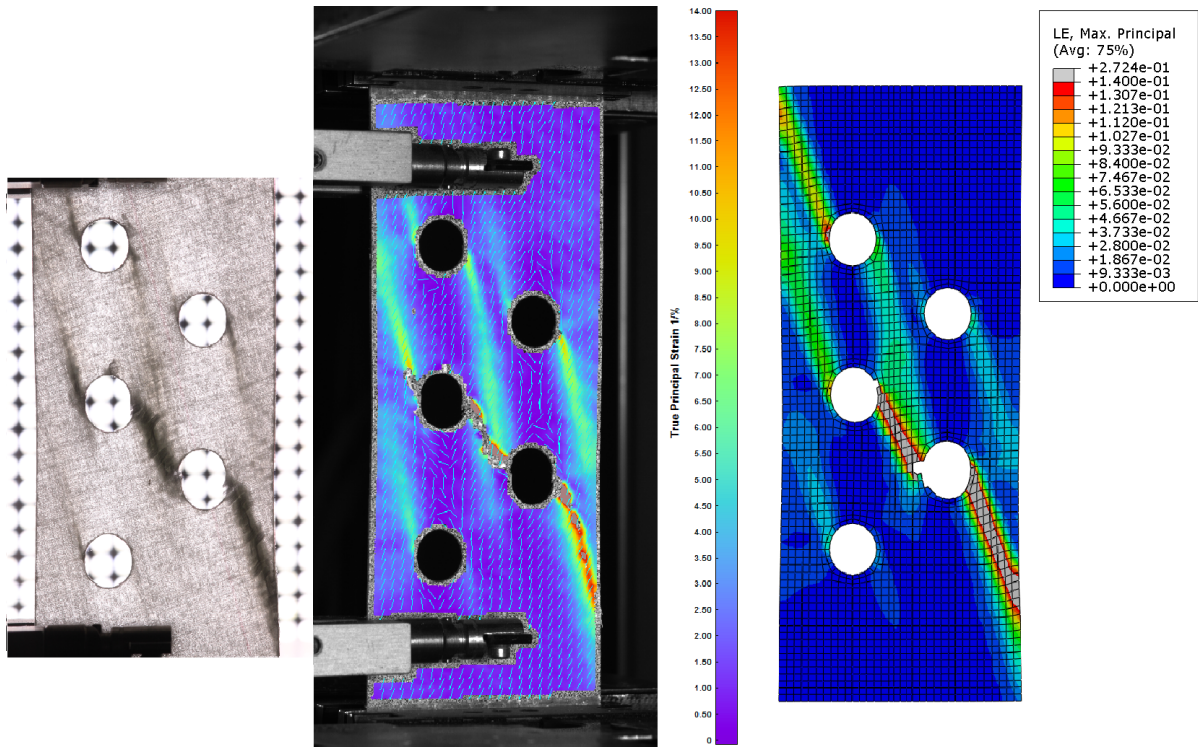


Fig. 8: Visual comparison of results for specimen TH-15 and displacement  $u = 2.0$  mm: the backlight illuminated specimen (left), the maximum true principal strain as resolved by the DIC system (center) and as computed by the numerical simulation (right)

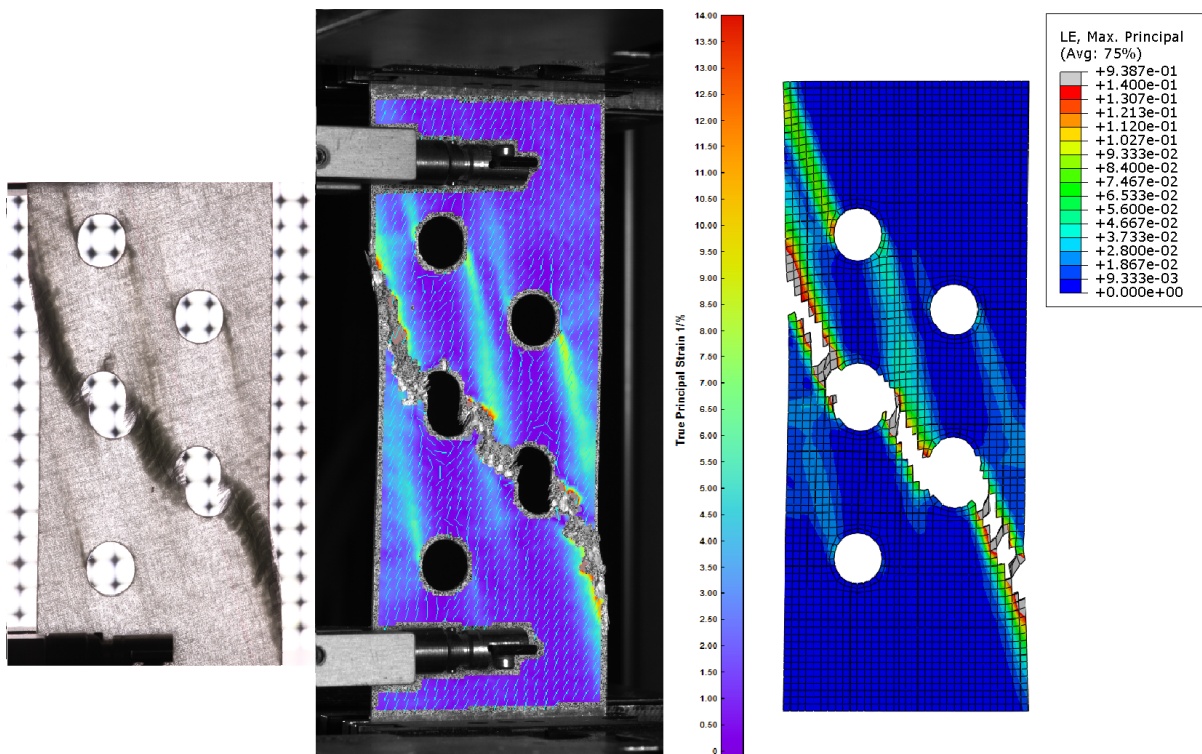


Fig. 9: Visual comparison of results for specimen TH-15 and displacement  $u = 4.0$  mm: the backlight illuminated specimen (left), the maximum true principal strain as resolved by the DIC system (center) and as computed by the numerical simulation (right)

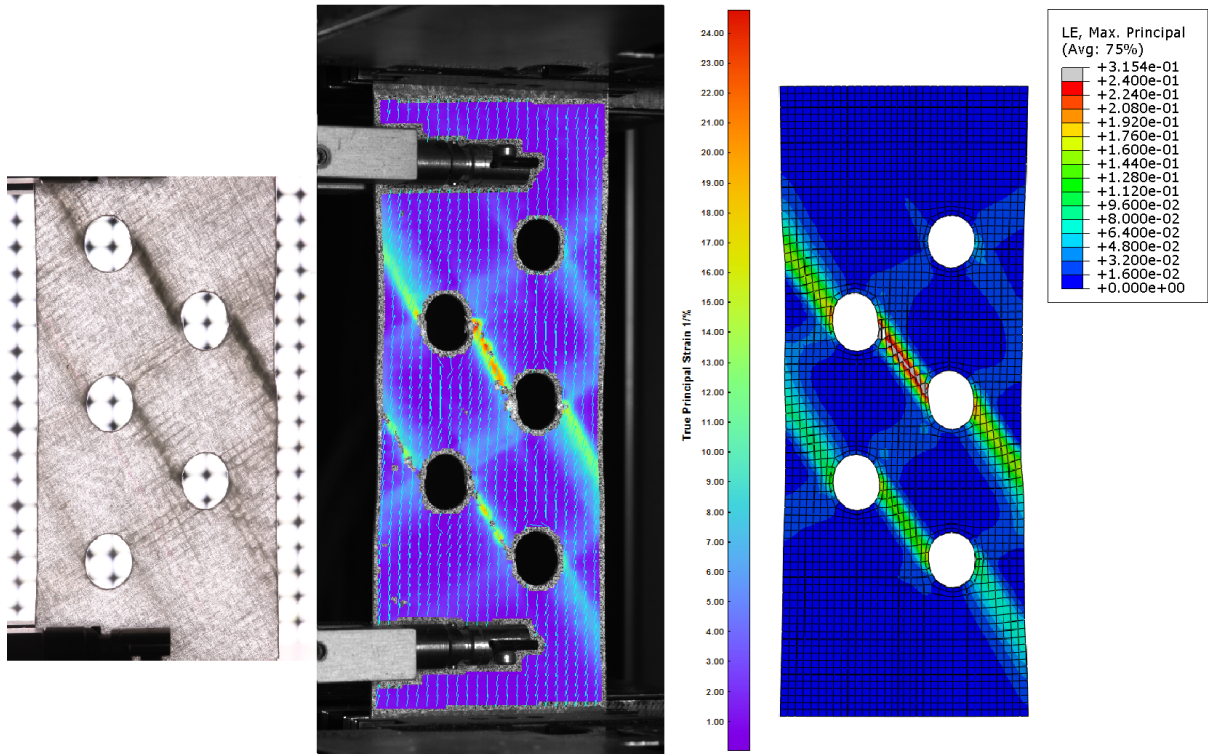


Fig. 10: Visual comparison of results for specimen TH-30 and displacement  $u = 3.0$  mm: the backlight illuminated specimen (left), the maximum true principal strain as resolved by the DIC system (center) and as computed by the numerical simulation (right)

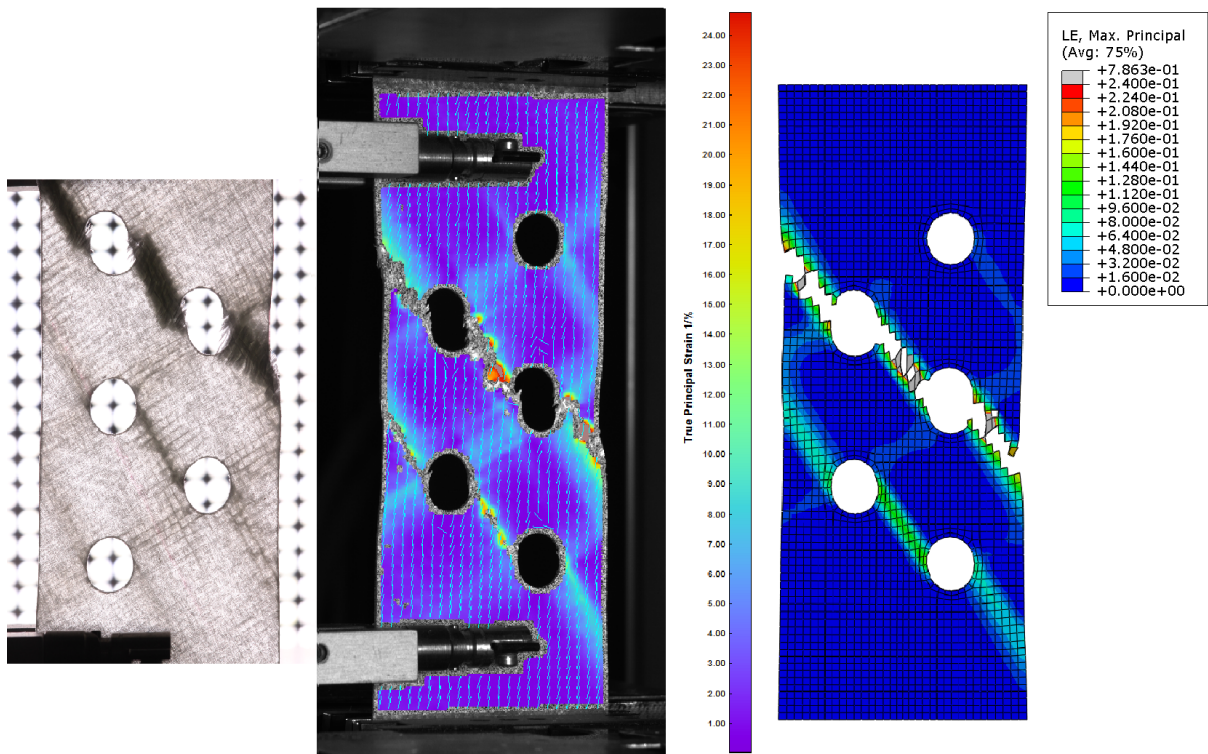


Fig. 11: Visual comparison of results for specimen TH-30 and displacement  $u = 4.0$  mm: the backlight illuminated specimen (left), the maximum true principal strain as resolved by the DIC system (center) and as computed by the numerical simulation (right)

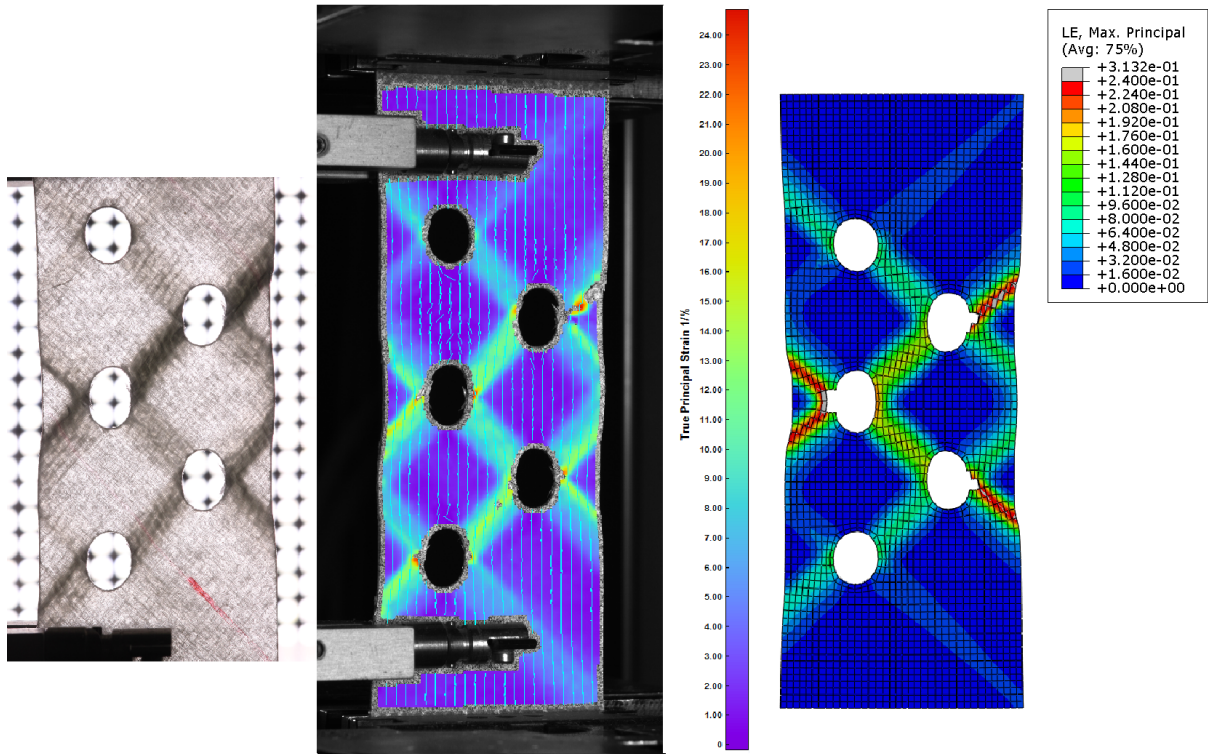


Fig. 12: Visual comparison of results for specimen TH-45 and displacement  $u = 5.0$  mm: the backlight illuminated specimen (left), the maximum true principal strain as resolved by the DIC system (center) and as computed by the numerical simulation (right)

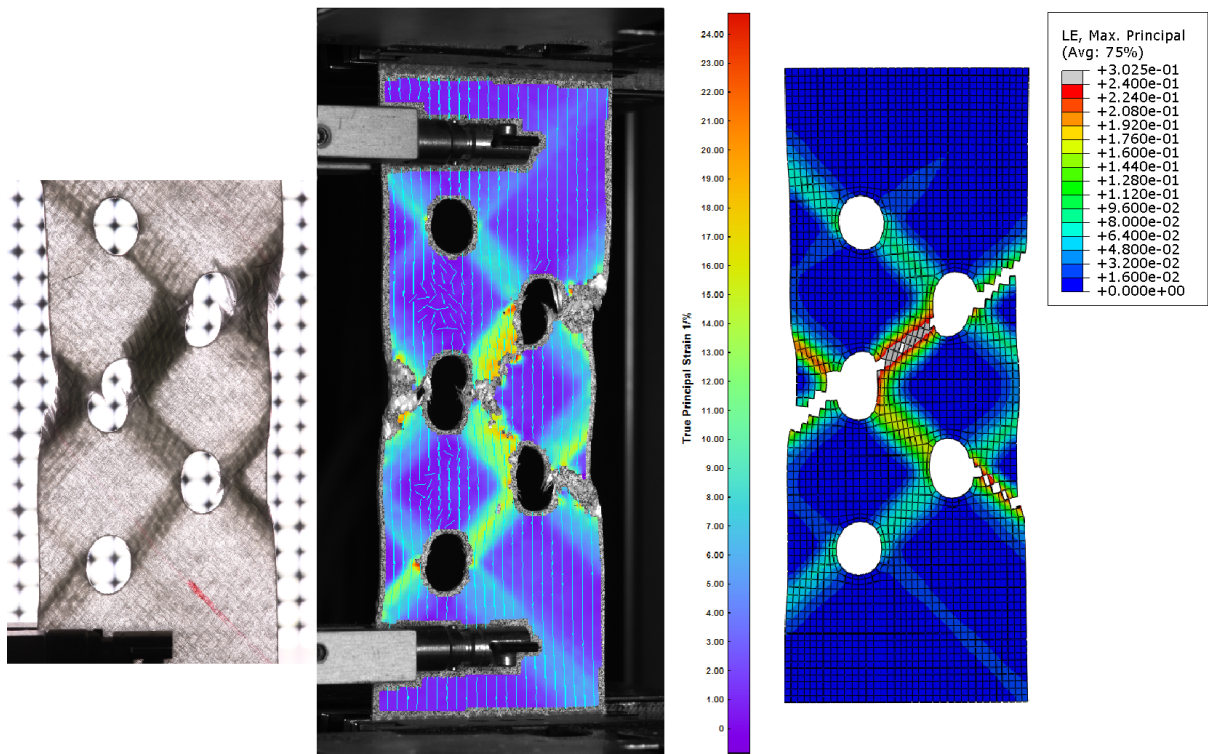


Fig. 13: Visual comparison of results for specimen TH-45 and displacement  $u = 7.0$  mm: the backlight illuminated specimen (left), the maximum true principal strain as resolved by the DIC system (center) and as computed by the numerical simulation (right)